frontiers in Physics

ORIGINAL RESEARCH
published: 19 January 2022
doi: 10.3389/fphy.2021.791459

Enhanced Measurement Accuracy for Nanostructures Using Hybrid Metrology

Poul-Erik Hansen, Sabrina Rostgaard Johannsen, Søren Alkærsig Jensen and Jonas Skovlund Møller Madsen*

Danish Fundamental Metrology A/S, Hørsholm, Denmark

Light-matter interplay is widely used for analyzing the topology of surfaces on small scales for use in areas such as nanotechnology, nanoelectronics, photonics, and advanced materials. Conventional optical microscope imaging methods are limited in resolution to a value comparable to the wavelength, the so-called Abbe limit, and cannot be used to measure nano-sized structures. Scatterometry and Mueller ellipsometry are spectroscopic optical methods that can measure structures smaller than the wavelength. However, the relative uncertainties of the structure dimensions measured with scatterometry increase with decreasing structure size, and the industry is therefore replacing simple intensity based scatterometry with Mueller ellipsometry for the most demanding measurements. The accuracy of Mueller ellipsometry and scatterometry are closely related to the ability of the employed regression and regularization algorithms to extract the structural dimension. In this work, we demonstrate how the measurement accuracy on three-dimensional periodic structures may be increased by measuring the same periodic structure with multiple techniques and applying a χ^2-regression method that finds the best solution based on the input from all the instruments. We furthermore report on a new and improved calibration method for Mueller ellipsometry and demonstrate how the Mueller matrix may be used to find the geometrical anisotropy of the structure.

Keywords: metrology, Mueller ellipsometry, inverse modelling, scatterometry, nanostructures

OPEN ACCESS

Edited by:
Ji Qi,
Imperial College London,
United Kingdom

Reviewed by:
Sébastien Robert Mouchet,
University of Exeter, United Kingdom
Alpan Bek,
Middle East Technical University,
Turkey

****Correspondence:***
Poul-Erik Hansen
peh@dfm.dk

Specialty section:
This article was submitted to Optics and Photonics, a section of the journal Frontiers in Physics

Received: *08 October 2021*
Accepted: *29 November 2021*
Published: *19 January 2022*

Citation:
Hansen P-E, Johannsen SR, Jensen SA and Madsen JSM (2022) Enhanced Measurement Accuracy for Nanostructures Using Hybrid Metrology. Front. Phys. 9:791459. doi: 10.3389/fphy.2021.791459

1 INTRODUCTION

Nanostructures have a wide array of applications in optics, diagnostics, food science, sensing, and process inspection monitoring. Some of these applications include enhancing waveguide coupling, improving linear encoders, making hyperspectral cameras and printing color images [1–4]. Imaging technologies like Optical Microscopy (OM), Atomic Force Microscopy (AFM) and Scanning Electron Microscopy (SEM) are the dominating quality assesment technologies in low volume, high-cost nanoscale manufacturing, whereas scatterometry and Mueller ellipsometry are the preferred technologies for high volume manufacturing. However, the measurement accuracy for all of the above-mentioned technologies is decreasing with the ever decreasing nanostructure sizes. OM cannot measure the shape of objects with lateral sizes less than 1 μm; AFM cannot accurately measure shape but can measure the nanostructure height if the separation width is longer than the tip width; lateral and vertical dimensions from SEM pictures are hard to obtain if the width of the borderline produced by the secondary electron becomes a significant part of the dimension to be measured [5]. Scatterometry and Mueller ellipsometry can measure the shape of periodic

nanostructures [6–8]; however, the accuracy of the shape dimensions decrease with decreasing nanostructure sizes and increasing complexity. We proposed to use hybrid metrology that combines scatterometry, Mueller ellipsometry, and AFM for shape reconstruction of nanostructures. Scatterometry can be defined as the measurement and analysis of light diffracted by structures using fixed polarization settings.

The scattered (or diffracted) light is a signature or "fingerprint" which reflects the details of the structure itself. For a periodic device, such as a series of lines and spaces in silicon, the scattered light consists of distinct diffraction orders at angular locations specified by the well-known grating equation. The fraction of the incident power diffracted into any order is sensitive to the shape and dimensional parameters of the diffracting structure and may therefore be used to characterize the structure itself [9]. This is done using a mathematical model of the structure based on a priori information and a rigorous simulation of the light-structure interaction. Rigorous Coupled Wave Analysis (RCWA) [10] is the common workhorse for scatterometry modelling due to its speed, convergence and relatively simple implementation. In RCWA, the nanostructure is approximated by rectangular slabs, and Maxwell's equations are solved by coupling the boundary conditions between the slabs. The dimensional parameters are obtained using a best-fit procedure between experimental data and calculated values [11].

Ellipsometry measures the polarization-dependent optical response from a sample [9]. In the conventional configuration, an amplitude and a phase parameter, describing the change in polarization in an isotropic sample, are measured. Mueller ellipsometry is a more advanced method, which may be further divided into two groups: Non-normalized Mueller ellipsometers that measure all 16 Mueller matrix elements, and normalized Mueller ellipsometers in which the 16 Mueller matrix elements are normalized with the first Mueller matrix element m_{11}. The sensitivity of Mueller ellipsometry comes from the measurement of both the magnitude and phase of the Fresnel response/reflection from the sample, and as a rule of thumb, the sensitivity increases with asymmetries and increased density of the structure. Furthermore, it is possible to use the same mathematical modelling method as in scatterometry. Several strategies exist for precision Mueller ellipsometry measurement and have been investigated by a number of authors [12–16]. A necessary prerequisite for high precision Mueller ellipsometry measurements is accurate calibration of the Mueller ellipsometer. We have developed a new calibration method consisting of a fast method for monitoring the most important experimental settings on a daily basis and a more comprehensive method for monitoring of the entire instrument. The method, explained in section 2.1, makes it possible to correct for fluctuation in the dominating experimental parameters on a much shorter timescale and easily monitor the linearity of the instrument response.

In this paper, we report on the progress of accurate determination of the dimensional parameters of three-dimensional periodic nanostructures by measuring the same periodic structure with multiple technologies and applying a χ^2-regression method with regularization that finds the best solution based on the input from all the instruments. We have measured a square patterned periodic grating with truncated cone shapes with a 200 nm period in the x and y direction, see **Figure 1**, using scatterometry, Mueller ellipsometry, and AFM. The χ^2-regression method contains two parts, the first part includes the scatterometry and Mueller ellipsometry contribution, while the second part is a Tikhonov regularization part used for including the AFM height measurement. We demonstrate that the hybrid metrology approach improves the accuracy of the obtained dimension. In particular, we observe an improvement for strongly correlated parameters. The paper is organized in the following way: In **Section 2**, we describe the experimental scatterometry and Mueller ellipsometry setups together with the newly developed method for calibration of the Mueller ellipsometer. In **section 3**, the forward model used for simulating the light-matter interaction is presented. In **section 4**, we explain the applied inverse method, showing how it is used to find the dimensional parameters and calculate the corresponding uncertainties. **Section 5** is devoted to the discussion of the obtained results, and **section 6** summarizes the results obtained.

2 MATERIALS AND METHODS

The experimental system is a combined goniometric and spectroscopic setup. In this work, we use only the

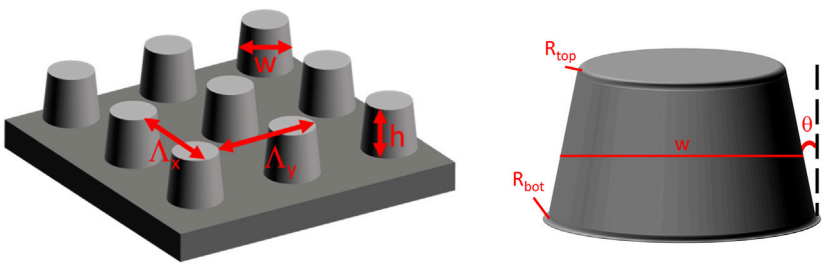

FIGURE 1 | Illustration of the truncated cone model and the parameterization used to describe the physical sample. The parameters (periods, Λ_x and Λ_y, height, h, and width, w) specified by the manufacturer are shown on the left, while the additional parameters used (sidewall angles, θ, and corner rounding radii, R_{top} and R_{bot}) are shown on the right. The width is defined as the full-width-half-max of the cone.

spectroscopic scatterometry and Mueller ellipsometry measurement modes. A sketch of the setup can be seen in **Figure 2**. As radiation source, we use a Laser-Driven Light Source (LDLS) (Energetiq, EQ-99X). The LDLS lamp covers a wavelength range from 170 to 2,200 nm. The light is focused onto a 150 μm pinhole using parabolic mirrors and secondly collimated by an UV-to-NIR corrected triplet lens (Edmund Optics, 180 mm). The collimated light passes through a polarization state generator (PSG) made from an α - BBO polarizer (Edmund Optics, 68–827) followed by a photo elastics modulator (PEM, Hinds Instrument, I/FS50). At this point the beam diameter is roughly 1.5 mm. The angle of incidence on the sample may be varied between +/- 90° via a rotation stage (Thorlabs, NR360S) equipped with angular encoder (Heidenhain, ERA 4200C). The detector arm can be scanned over nearly the complete diffraction plane, +/- 175°, and is equipped with a polarization state analyzer (PSA), made from a photo elastic modulator (Hinds Instrument, I/FS60) and an α - BBO polarizer (Edmund Optics, 68–827), followed by a spatial mirror (Thorlabs, RC08APC-P01) that focuses the light into a fiber coupled monochromator (Spectral products, DK242). The monochromator is equiped with two gratings, a UV-optimized grating for wavelengths below 400 nm and another for the wavelengths above. The output from the monochromator is focused on a PMT detector (Hamamatsu, R928P). The detected signal is split into a DC and an AC signal using an analog filter (SIM 965, Stanford Research System) with a low-pass frequency cut at 30 Hz. The DC signal is fed into an analog PID controller (SIM 960, Stanford Research System) that together with a custom build PMT amplifier, controls the high voltage power supply (PS 310, Stanford Research System) of the PMT such that the recorded signal is always taken at the same DC value ((1.35 ± 0.005) V in the presented work). A digitizer (Agilent L4534A) is used for simultaneous sampling of the recorded signal together with the PSG and PSA waveforms. The waveforms are long-pass filtered at 1 MHz and voltage limited to +/- 8 V in the digitizer prior to data analysis. By rotating these PEMS to different angles (labeled θ_{m_0} and θ_{m_1}), one can probe different elements of the Mueller Matrix. The PEM waveforms and the signal are analyzed by fast Fourier transformation. **Eq. 4** in the **Supplementary Material** of ref. [17] shows that the recorded Mueller ellipsometer signal may be written as a Fourier expansion of frequencies in the following way:

$$\begin{aligned} I = I_{DC} &+ I_{f_0}\cos\left(\omega_0 t + \phi_0 - \frac{\pi}{2}\right) + I_{f_1}\cos\left(\omega_1 t + \phi_1 - \frac{\pi}{2}\right) \\ &+ I_{2f_0}\cos\left(2\omega_0 t + 2\phi_0\right) + I_{2f_1}\cos\left(2\omega_1 t + 2\phi_1\right) \\ &+ I_{f_0+f_1}\cos\left((\omega_0+\omega_1)t + \phi_0 + \phi_1\right) \\ &+ I_{2f_0+f_1}\cos\left((2\omega_0+\omega_1)t + 2\phi_0 + \phi_1 - \frac{\pi}{2}\right) \\ &+ I_{f_0+2f_1}\cos\left((\omega_0+2\omega_1)t + \phi_0 + 2\phi_1 - \frac{\pi}{2}\right) \\ &+ I_{2f_0+2f_1}\cos\left((2\omega_0+2\omega_1)t + 2\phi_0 + 2\phi_1\right) + \ldots \end{aligned} \quad (1)$$

Where $\omega_i = 2\pi f_i$, $i = 0, 1$ and ϕ_0, ϕ_1 are the angular frequencies and phases of the photo elastic modulators. I_{f_i} are the amplitudes and I_{DC} is the DC value that is kept constant for all measurements. The measurands obtained from Fourier transformation of the signal are:

$$\begin{aligned} I_{DC} \quad \text{and} \quad I_{f_i}, f_i \in \{&f_0,\ f_1,\ 2f_0,\ 2f_1,\ f_0+f_1,\ 2f_0 \\ &+f_1,\ f_0+2f_1,\ 2f_0+2f_1\} \end{aligned} \quad (2)$$

It is demonstrated in [17] that the nine measurands in **(2)** give a complete description of the signal, I, in **Eq. 1**. The normalized intensities $A_{f_i} = I_{f_i}/I_{DC}$ can be directly related to the Mueller matrix elements as explained in **section 2.1**, and the 15 normalized Mueller matrix elements may be obtained by measuring A_{f_i} for different angular positions of the PSG (θ_{m_0}) and PSA (θ_{m_1}). The Muller ellipsometry data obtained are normalized with the m_{11} Mueller matrix element. The Mueller matrix element, m_{11}, can be measured using scatterometry. During the scatterometry measurements, the PEMs were not oscillating and the outgoing light was connected via fiber to a UV to NIR spectrometer (Ocean optics, FLAME-S-XR1-ES) instead of the monochromator.

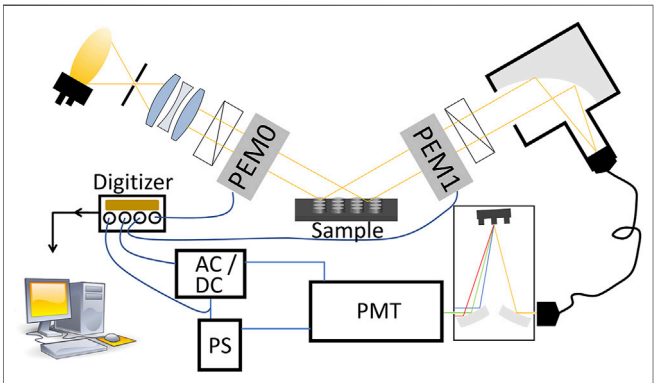

FIGURE 2 | Schematic illustration of the experimental setup. The main components are the light source, the two photo elastic modulators (PEM0 and PEM1), a monochromator and a detection system based on a photomultiplier tube (PMT), a high voltage power supply (PS) and electronics measuring the AC and DC components of the signal (AC/DC).

2.1 Data Acquisition and Calibration Method for Mueller Ellipsometry

The details of the data acquisition are explained in the **Supplementary Material**. Here we continue by showing how precision calibration of the setup can be made prior to measurement. The main results of this section are **Eqs 4**, **6**. **Eq. 4** presents new expressions for improving the measured Bessel amplitudes, and **Eq. 6** is a high precision formulation of the standard formulas in [15]. The notation used in the derivations are similar to the one used in [15]. The prior-to-measurement calibration is by far the most important calibration since PEMs are very stable devices. However, regular system calibration is needed to monitor the performance of the entire system, and a simple method for this is described in the **Supplementary Material**.

The quantities measured with the Mueller ellipsometry setup are the eight normalized intensities $A_{f_i} = I_{f_i}/I_{DC}$, see (2). In this section we show that the normalized intensities A_{f_i} are well defined functions of the Mueller matrix elements (m_{ij}), the Bessel amplitudes (A_0, A_1) and the static strain (δ_0, δ_1) of the PEM phase retardation, the two polarizer angles (θ_{p_0}, θ_{p_1}), the two PEM angles (θ_{m_0}, θ_{m_1}) used to select the Mueller matrix elements of interest, and the Bessel functions of the first kind J_n. With a suitable choice of polarizer and PEM angles, a normalized intensity A_{f_i} is dominated by a single Mueller matrix element as indicated in **Eq. 6**. However, the influences of other Mueller matrix elements are only eliminated if all the Bessel amplitudes A_0, A_1 have been adjusted so that $J_0(A_0) = J_0(A_1) = 0$ (e.g. $A_0 = A_1 = 2.404\,8$), if the static strains δ_0, δ_1 are zero, and if all polarizers and PEM angles are perfectly set. This optimal situation can hardly be obtained in practice, so precise calibrations are needed. We perform a system calibration in which all of the system is calibrated, and a prior-to-measurement calibration of the Bessel amplitudes and the static strain. During calibration, we find the optimal voltages for each PEM in order to make sure that the value of A_0 and A_1 are within the range from 2.28 to 2.38 for all the measured wavelengths. This range ensures that we are within the linear range of the Bessel functions and safely away from the point where J_0 changes sign. In practice, this is done by making a calibration function (polynomial of second degree) for each combination of PEM and monochromator grating, resulting in four wavelength-voltage calibration functions. The measurement of the Bessel amplitudes is obtained from transmission calibration measurements without sample in the Mueller ellipsometer, using $\theta_{p_0} \approx \theta_{p_1} \approx -45^\circ$ and $\theta_{m_0} \approx \theta_{m_1} \approx 0^\circ$ and assuming $J_0(A_0) \approx J_0(A_1) \approx 0$, so that we can expand the Bessel function as

$$\begin{aligned} J_0(A_0) &\approx C\left(A_p - A_0\right) \\ J_0(A_1) &\approx C\left(A_p - A_1\right) \end{aligned} \tag{3}$$

where $C = 0.519\,6$ and $A_p = 2.4048$. After derivation, see **Supplementary Material**, we find the following very useful expressions for A_0 and A_1

$$\begin{aligned} A_0 &= A_p - \frac{A_{2f_1}}{2CD\left(J_2\left(A_p\right) + \left(J_1\left(A_p\right) - J_3\left(A_p\right)\right)\dfrac{A_{2f_0}}{4CDJ_2\left(A_p\right)}\right)} \\ A_1 &= A_p - \frac{A_{2f_0}}{2CD\left(J_2\left(A_p\right) + \left(J_1\left(A_p\right) - J_3\left(A_p\right)\right)\dfrac{A_{2f_1}}{4CDJ_2\left(A_p\right)}\right)} \end{aligned} \tag{4}$$

where $D = \cos(2(\theta_{m_1} - \theta_{m_0})) \approx \pm 1$ is a measure of the relative angular position of the PEMs. **Eq. 4** is very important for high precision measurements since the normalized intensities A_{f_i} are strongly dependent on the correct values for the Bessel amplitudes. The static strain measurement is performed in order to see if the assumption δ_0, $\delta_1 \approx 0$ holds for all wavelengths, the measurements are performed by setting $\theta_{p_0} \approx -45^\circ$, $\theta_{p_1} \approx 0$, $\theta_{m_0} \approx 0$, $\theta_{m_1} \approx -45^\circ$ and measuring $A_{2f_0+f_1}$, $A_{f_0+2f_1}$,

$$\begin{aligned} \delta_0 &= \frac{A_{2f_0+f_1}\left(1 + C_{b_0}C_{b_1}C_{m_0}C_{m_1} + C_{b_0}S_{m_0} + C_{b_0}C_{b_1}S_{m_0}S_{m_1}\right)}{-2J_2(A_0)J_1(A_1)} \\ \delta_1 &= \frac{A_{2f_1+f_0}\left(1 + C_{b_0}C_{b_1}C_{m_0}C_{m_1} + C_{b_0}S_{m_0} + C_{b_0}C_{b_1}S_{m_0}S_{m_1}\right)}{-2J_2(A_1)J_1(A_1)} \end{aligned} \tag{5}$$

where $C_{b_0} = \cos(2(\theta_{m_0} - \theta_{p_0}))$, $C_{b_0} = \cos(2(\theta_{m_1} - \theta_{p_1}))$, $C_{m_0} = \cos(2\theta_{m_0})$, $C_{m_1} = \cos(2\theta_{m_1})$, $S_{b_0} = \sin(2(\theta_{m_0} - \theta_{p_0}))$, $S_{b_0} = \sin(2(\theta_{m_1} - \theta_{p_1}))$, $S_{m_0} = \sin(2\theta_{m_0})$ and $S_{m_1} = \sin(2\theta_{m_1})$. **Figure 3** shows typical Bessel amplitude and static strain values for the measurement system. Assuming that δ_0, $\delta_1 \approx 0$, $S_{b_0} = \pm 1_{b_0}$, $S_{b_1} = \pm 1_{b_1}$, $C_{b_0} = 0$ and $C_{b_1} = 0$, like in most setups, we can write the expressions that relate the normalized intensity $A_{f_i} = \frac{I_{f_i}}{I_{DC}}$ and the Mueller matrix elements, m_{ij}

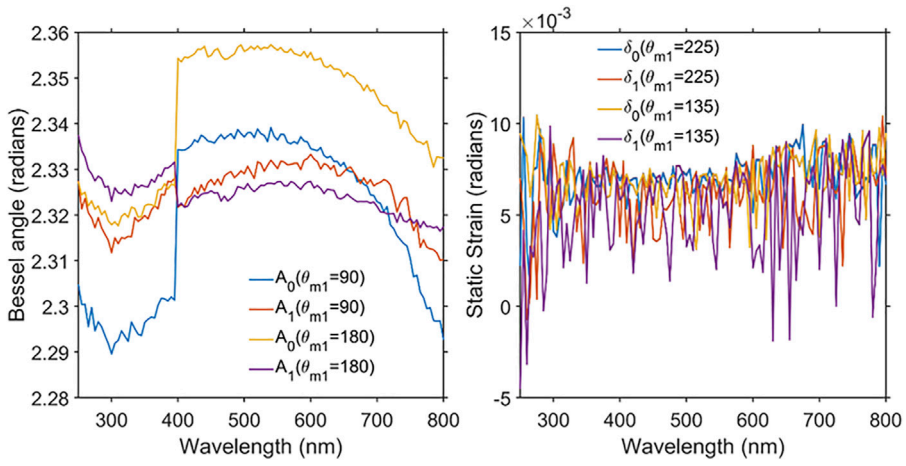

FIGURE 3 | Typical Bessel amplitudes A_0, A_1 and static strains δ_0, δ_1 as a function of wavelength. We note that the Bessel amplitudes are in the desired range from 2.28 to 2.38. A jump is seen around the wavelength of 400 nm, where the monochromator grating and PEM calibration function is changed.

$$
\begin{aligned}
A_{f_0} &\approx 2J_1(A_0)m_{14}(\pm 1_{b_0})\frac{I_{DC}}{I_{DC_0}}\\
A_{f_1} &\approx 2J_1(A_1)(-m_{41}(\pm 1_{b_1}))\frac{I_{DC}}{I_{DC_0}}\\
A_{2f_0} &\approx 2J_2(A_0)(-m_{13}C_{m_0}(\pm 1_{b_0}) + m_{12}(\pm 1_{b0})S_{m_0})\frac{I_{DC}}{I_{DC_0}}\\
A_{2f_1} &\approx 2J_2(A_1)(-m_{31}C_{m_1}(\pm 1_{b_1}) + m_{21}(\pm 1_{b_1})S_{m_1})\frac{I_{DC}}{I_{DC_0}}\\
A_{f_0+f_1} &\approx -2J_1(A_0)J_1(A_1)(-m_{44}(\pm 1_{b0})(\pm 1_{b1}))\frac{I_{DC}}{I_{DC_0}}\\
A_{2f_0+f_1} &\approx 2J_1(A_1)J_2(A_0)(-m_{42}S_{m_0}(\pm 1_{b_0})(\pm 1_{b_1})\\
&\quad +m_{43}C_{m_0}(\pm 1_{b_0})(\pm 1_{b_1}))\frac{I_{DC}}{I_{DC_0}}\\
A_{f_0+2f_1} &\approx 2J_1(A_0)J_2(A_1)(m_{24}(\pm 1_{b_0})(\pm 1_{b_1})S_{m_1}\\
&\quad -m_{34}C_{m_1}(\pm 1_{b_0})(\pm 1_{b_1}))\frac{I_{DC}}{I_{DC_0}}\\
A_{2f_0+2f_1} &\approx 2J_2(A_0)J_2(A_1)(-m_{32}C_{m_1}(\pm 1_{b_0})(\pm 1_{b_1})S_{m_0}\\
&\quad + m_{33}C_{m_0}C_{m_1}(\pm 1_{b_0})(\pm 1_{b_1})+\\
&\quad m_{22}(\pm 1_{b_0})(\pm 1_{b_1})S_{m_0}S_{m_1} - m_{23}C_{m_0}(\pm 1_{b_0})(\pm 1_{b_1}))S_{m_1}\frac{I_{DC}}{I_{DC_0}}
\end{aligned}
\tag{6}
$$

where the ratio between the correct DC value and the measured DC value $\left(\frac{I_{DC_0}}{I_{DC}}\right)$ is given by,

$$
\begin{aligned}
\frac{I_{DC_0}}{I_{DC}} &\approx 1 - \frac{C\left((A_p - A_0)(-m_{13}C_{m_0}(\pm 1_{b_0}) + m_{12}(\pm 1_{b0})S_{m_0}) + (A_p - A_1)(-m_{31}C_{m_1}(\pm 1_{b_1}) + m_{21}(\pm 1_{b_1})S_{m_1})\right)}{I_{DC}}\\
&\approx 1 - \frac{C\left((A_p - A_0)\frac{A_{2f_0}}{2J_2(A_0)} + (A_p - A_1)\frac{A_{2f_1}}{2J_2(A_1)}\right)}{I_{DC}}.
\end{aligned}
\tag{7}
$$

Eq. 7 demonstrates that the correction term vanishes for perfect Bessel amplitudes and that it gets less important with higher I_{DC} values. A high value and low variation are thus optimal. In this paper, we have used a value of (1.350 ± 0.005) V. The calibration Mueller matrix is the Mueller matrix of air, which is a non-depolarizing Mueller matrix. However, the measured calibration Mueller matrix may be influenced by small depolarization $(0.98 < \beta(\lambda) < 1)$ from the components in the setup, for $\lambda > 300$ nm. This depolarization may be found from the following formula [18–20]:

$$
\frac{1}{\beta^2(\lambda)}\sum_{i,j=1}^{4} m_{ij}^2(\lambda) = 4m_{11}^2(\lambda). \tag{8}
$$

The measured Mueller matrix, with the sample in place, is renormalized with the instrument depolarization in order to exclude the influence of the system components in the data fitting. The beta values are shown in **Figure 4**. For the sample, we see a large dip for wavelenghts below 300 nm. This is attributed to our signal quality in this spectral region. We have increased the measurement uncertainty in this region to lower the effect on the final measurement.

2.2 Sample and Measurements

A periodic patterned silicon structure $\Gamma_x = \Gamma_y = 200$ nm was purchased from Eulitha AG.

The Mueller ellipsometry measurements were performed at 70° angle of incidence, and 15 Mueller matrix elements have been measured by performing measurements at PSG angles, $\theta_{m_0} = [180, 135, 135, 180]^\circ$ and PSA angles $\theta_{m_1} = [135, 135, 180, 90]^\circ$. The Mueller matrix elements were calculated from the measured intensities in **(2)** following the procedure described in section 2.1 and in the **Supplementary Material**. Scatterometry measurements $I(\lambda)$ were also performed at a 70° angle of incidence together with a reference measurement $I_{ref}(\lambda)$ taken on a flat piece of Si100, and a dark measurement $I_{dark}(\lambda)$ obtained by blocking the light source. The light was polarized perpendicular to the incidence plane during all measurements. The diffraction efficiencies, $\eta(\lambda)$, are calculated from the three scatterometry measurements in the following way:

$$
\eta(\lambda) = R(\lambda)\frac{I(\lambda) - I_{dark}(\lambda)}{I_{ref}(\lambda) - I_{dark}(\lambda)} \tag{9}
$$

where $R(\lambda)$ is the wavelength-dependent reflection coefficient of the material used for the reference measurement.

For the AFM measurements of the heights of the gratings, we used a metrology AFM (Park Systems, NX20, Suwon, South Korea) in tapping mode, equipped with Point Probe Plus tips (Nanosensors), with a specified apex radius < 10 nm. The AFM has an xy-stage equipped with optical distance sensors and a z-flexure stage equipped with strain gauge distance sensors. The microscope was calibrated in the z-direction using a step height standard as described in [21]. The area measured by the AFM was well within the area covered by the beam spot in the optical measurements. The images were analyzed using the step height module in Scanning Probe Image Processor (SPIP) (ver. 6.7.3, Image Metrology) and following the ISO 5436 standard for measuring step heights. We stress that only the height is measured by the AFM. Following this standard, we eliminate the effect of sample-tip convolution on the measured height.

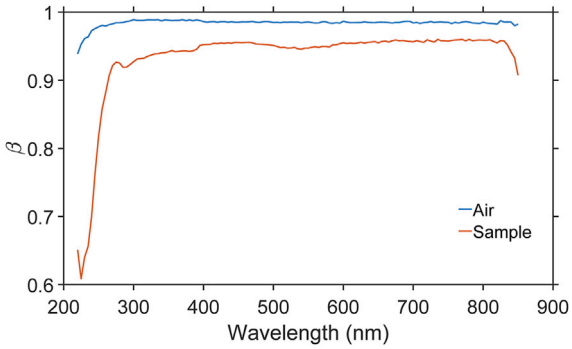

FIGURE 4 | Measured values of the depolarization β with and without a sample (Air). For wavelengths below 300 nm, we see a steep drop for the sample measurements, which is not present in the air measurement. This demonstrates sample depolarization for lower wavelengths. The depolarization measured without the sample is referred to as the instrument depolarization.

2.3 RCWA for Nanostructure Characterization

Light scattering from the periodic patterened nanostructure is modeled by rigorously solving Maxwell's equations in the

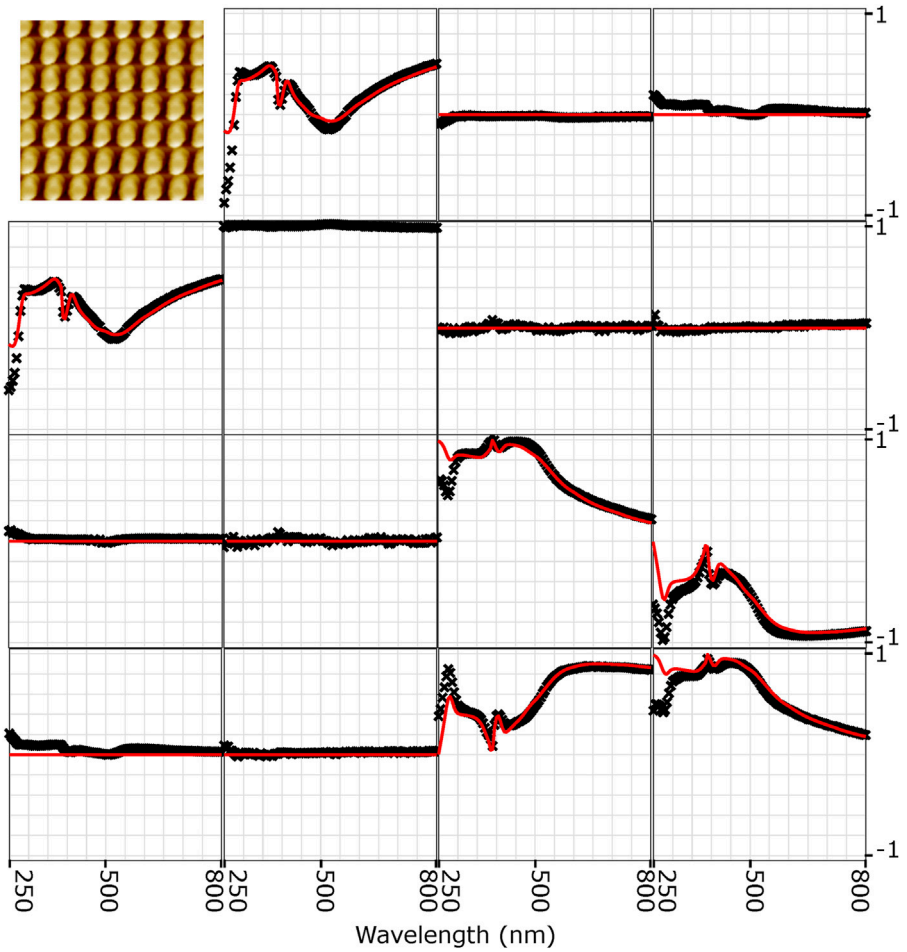

FIGURE 5 | Experimental Mueller ellipsometry measurements (black crosses) and fitted Mueller ellipsometry results (red lines). The upper left corner shows an AFM picture of the structure. A strong agreement between model and fit are found within all Mueller matrix elements for wavelengths > 300 nm. All the anisotropic Mueller matrix elements: m_{13}, m_{14}, m_{23}, m_{24}, m_{31}, m_{32}, m_{41} and m_{42} have been set to zero in the model.

relevant frequency domain. The rigorous coupled-wave (RCWA) software described in [11] has been extended to handle arbitrary repeated profiles with complex material distributions. The profile is approximated by division into multiple slabs. Each slab consists of N_q building blocks that all have the same height h_q. Each building block within a slab is furthermore labeled with an index i. Each building block $b(q, i)$ is then characterized by its widths $w_x(q, i)$, $w_y(q, i)$ and offsets $x(q, i)$, $y(q, i)$ in the x- and y direction, respectively. Furthermore, each block is characterized by its permittivity $\epsilon(q, i)$ and permeability $\mu(q, i)$. The lateral periodicities of the slabs are given by the periodicity of the microstructure.

The new software runs within the Matlab environment and is used for forward calculations of the diffracted fields and efficiencies. The model structure used in the forward calculation is based on a priori information from the sample manufacturer, together with scanning electron microscope images of similar structures. These investigations showed that the nanostructure could be represented by the truncated cone geometry shown in **Figure 1**. The periodic truncated cone geometry may be characterized by a set of geometrical quantities $\mathbf{a}_0$ (e.g. period Γ_x, Γ_y height h, width w, sidewall angle θ, an oxide layer of thickness d, and corner radii R_1 and R_2). The Fresnel reflection coefficients r_{pp}, r_{sp}, r_{ps}, r_{ss} are calculated using RCWA as function of wavelength λ, angle of incidence θ, azimuth angle ϕ of the nanostructure relative to the scattering plane, refractive index $n + ik$ of the material, and for a specified set of geometrical sample quantities $\mathbf{a}_0$. The Fresnel coefficients from the RCWA simulations are related to the Mueller matrix by

$$M = \begin{pmatrix} 1 & 0 & 0 & 1 \\ 1 & 0 & 0 & -1 \\ 0 & 1 & 1 & 0 \\ 0 & -i & i & 0 \end{pmatrix} \left(\begin{pmatrix} r_{pp} & r_{ps} \\ r_{sp} & r_{ss} \end{pmatrix} \otimes \begin{pmatrix} r_{pp}^{*} & r_{ps}^{*} \\ r_{sp}^{*} & r_{ss}^{*} \end{pmatrix} \right) \begin{pmatrix} 1 & 0 & 0 & 1 \\ 1 & 0 & 0 & -1 \\ 0 & 1 & 1 & 0 \\ 0 & -i & i & 0 \end{pmatrix}^{-1} \tag{10}$$

where ⊗ denotes the Kronecker product and * denotes complex conjugation. The full polarization properties of a sample are contained in the 4 × 4 Mueller matrix (M), which for oblique incidence relates the Stokes vectors of the incident (S_i) and reflected (S_r) directions.

$$S_r = MS_i \tag{11}$$

In this work, we use normalized elements and $m_{11} \equiv 1$. The Stokes vector has the components

$$S_r = \begin{pmatrix} I \\ Q \\ U \\ V \end{pmatrix} = \begin{pmatrix} I_p + I_s \\ I_p - I_s \\ I_{+45} - I_{-45} \\ I_R - I_L \end{pmatrix} \tag{12}$$

where I_p, I_s, I_{+45}, and I_{-45} are, respectively, the irradiances of polarized light components parallel (p), perpendicular (s), at +45° and at -45° relative to the plane of incidence; I_R and I_L are the intensities of right- and left-handed circularly polarized light.

2.4 Inverse Modelling Method

Generally speaking, the inverse problem we consider is the task of calculating from a set of measurements the dimensional parameters that produced those results. Several techniques can be applied to solve inverse problems [10, 11]. The approach used here is based on setting up a regression problem in the following sense: Given a vector of measurement data $y \in R^n$, an RCWA model function, f_{RCWA}, that maps the parameter, $p \in R^m$, describing the truncated cone geometry that we want to determine to the measurement space f_{RCWA}: $R^m \rightarrow R^n$. The mapping function maps the parameter p into calculated scatterometry diffraction efficiencies (η^c) and calculated Mueller ellipsometry parameters (m_{ij}^c), resulting in an approximation of the measurement data. If one has additional knowledge about the measurement errors, e.g. if one knows the variances σ_i^2 of each of the measured values y_i, one can use this knowledge to weight the different measurements accordingly, hence limiting the influence of observations that are expected to have a large error. If more knowledge of the parameters p exists from other experiments, this knowledge may be incorporated into the χ^2-function as a penalty term. The most common penalty terms are Bayesian and Tikhonov regularization. Tikhonov regularization can be used to incorporate measurands of one or more parameters included in p from other instruments in a direct and appealing way. The χ^2-regularization method used in this work contains two parts, the scatterometry and Mueller ellipsometry contribution and the AFM height measurement. The latter is incorporated as a Tikhonov regularization used to penalize the model from fitting a height, h_c, different than the height, h, measured by AFM.

$$\begin{aligned}\chi^2(p) \;=\; & \frac{1}{2}\left(\frac{(h-h^c)^2}{\sigma_{AFM}^2} + \frac{1}{7N}\sum_{i=1}^{N}\left[\frac{\left(m_{12}(\lambda_i) - m_{12}^c(\lambda_i,p)\right)^2}{\sigma_{m_{12}}(\lambda_i)^2}\right.\right. \\ & + \frac{\left(m_{21}(\lambda_i) - m_{21}^c(\lambda_i,p)\right)^2}{\sigma_{m_{21}}(\lambda_i)^2} + \frac{\left(m_{33}(\lambda_i) - m_{33}^c(\lambda_i,p)\right)^2}{\sigma_{m_{33}}(\lambda_i)^2} \\ & + \frac{\left(m_{44}(\lambda_i) - m_{44}^c(\lambda_i,p)\right)^2}{\sigma_{m_{44}}(\lambda_i)^2} + \frac{\left(m_{34}(\lambda_i) - m_{34}^c(\lambda_i,p)\right)^2}{\sigma_{m_{34}}(\lambda_i)^2} \\ & \left.\left. + \frac{\left(m_{43}(\lambda_i) - m_{43}^c(\lambda_i,p)\right)^2}{\sigma_{m_{43}}(\lambda_i)^2} + \frac{\left(\eta(\lambda_i) - \eta^c(\lambda_i,p)\right)^2}{\sigma_{\eta}(\lambda_i)^2}\right]\right)\end{aligned} \tag{13}$$

where the superscript c indicates calculated values, and N is the number of wavelengths. The above equation can be minimized by applying a combination of global and local optimization algorithms, in our case we use differential evolution as a global optimization method [22] and the Levenberg-Marquardt method for local optimization. Once we have determined the best fit, we can also estimate the uncertainties, $u(p)$, from the diagonal elements of the covariance matrix (Σ) using

$$\Sigma = \left(\boldsymbol{J}^T U^{-1} \boldsymbol{J}\right)^{-1} \tag{14}$$

where U is a matrix containing all the squared measurement uncertainties in the diagonal while all other entries are zero, and $\boldsymbol{J}$ is the Jacobian of the elements m_{ij}^c, η^c and h^c in **Eq. 13** with respect to the truncated cone parameters; height (h), width (w), and sidewall angle (θ). $\boldsymbol{J}$ be expressed as

$$\boldsymbol{J} = \begin{bmatrix} \frac{\partial m_{ij}^c(\lambda_1)}{\partial h} & \frac{\partial m_{ij}^c(\lambda_1)}{\partial w} & \frac{\partial m_{ij}^c(\lambda_1)}{\partial \theta} \\ \vdots & \vdots & \vdots \\ \frac{\partial m_{ij}^c(\lambda_N)}{\partial h} & \frac{\partial m_{ij}^c(\lambda_N)}{\partial w} & \frac{\partial m_{ij}^c(\lambda_N)}{\partial \theta} \\ \frac{\partial \eta^c(\lambda_1)}{\partial h} & \frac{\partial \eta^c(\lambda_1)}{\partial w} & \frac{\partial \eta^c(\lambda_1)}{\partial \theta} \\ \vdots & \vdots & \vdots \\ \frac{\partial \eta^c(\lambda_N)}{\partial h} & \frac{\partial \eta^c(\lambda_N)}{\partial w} & \frac{\partial \eta^c(\lambda_N)}{\partial \theta} \\ \frac{\partial h^c}{\partial h} & \frac{\partial h^c(\lambda_n)}{\partial w} & \frac{\partial h^c}{\partial \theta} \end{bmatrix} \tag{15}$$

3 RESULTS AND DISCUSSION

The fitting of the Mueller ellipsometer and scatterometry signal for the silicon structures was performed as described in the previous sections and the results are shown in **Figure 5** and **Figure 6**.

The nonzero values of the elements in the off-diagonal blocks of the Mueller-matrix in **Figure 5** allow for an investigation of their interrelationships. A careful inspection provides the following relationships for all wavelengths: $m_{12} = m_{21}$, $m_{13} = m_{31}$, $m_{14} = m_{41}$, $m_{23} = m_{32}$, $m_{24} = m_{42}$, $m_{34} = -m_{43}$, $m_{33} = m_{44}$ leading to 8 unique elements that are reduced to 7 independent elements by **Eq. 8**. Of particular interest is when the sample is illuminated with unpolarized light $S_i = [1,0,0,0]^T$ (T denotes transpose). In this case according to **Eq. 11**, the Stokes vector of the reflected beam is determined from the elements in the first column of the Mueller-matrix $S_r = [1, m_{21}, m_{31}, m_{41}]^T$, the so-called polarizance of the sample. It can be noticed that $m_{31} = 0$, $m_{21} \neq 0$, and $m_{41} > 0$, indicating that the incident light is reflected with right-handed polarization, and that the most positive values of m_{41} are found at low wavelengths. This conversion is possible if the sample has periodic structural anisotropy such that TE and TM waves experience different refractive indices (form birefringence

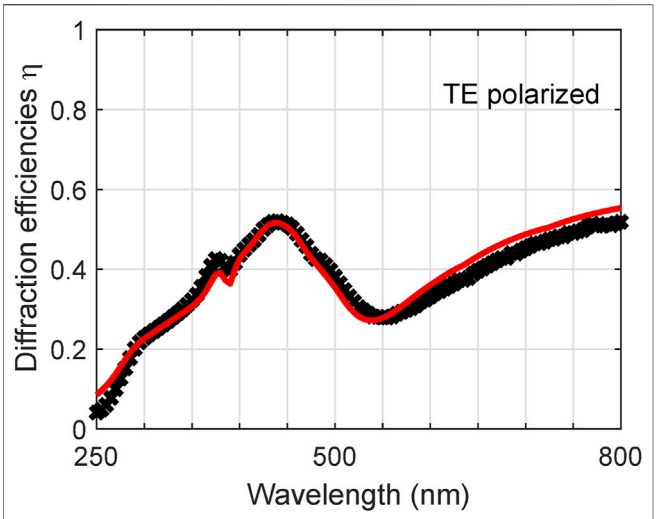

FIGURE 6 | Experimental scatterometry data (black crosses) and the corresponding optimal η^c found by minimizing the expression in **Eq. 13** (red line).

[23]. The state of polarization of light can be visualized with the polarization ellipse and explained by two parameters: the ellipticity e and the azimuth angle ϕ. We will also use the ellipticity angle $\varepsilon = \arctan(e)$. The parameters ε and ϕ are related to the Stokes vector S in **Eq. 11**, which for the special case of incident unpolarized light can be expressed as [24].

$$\varepsilon = \frac{1}{2}\arcsin\left(\frac{m_{41}}{\sqrt{m_{21}^2 + m_{31}^2 + m_{41}^2}}\right)$$
$$\phi = \arctan\left(\frac{m_{21}}{m_{31}}\right). \tag{16}$$

Eq. 16 yields $e \approx 0.1$ and $\phi \approx \frac{\pi}{2}$. We are thus lead to the conclusion that the truncated cone in **Figure 1** is not completely symmetric, but has shape anisotropy in the y-direction. We believe that it is this anisotropy that gives rise to the generally observed disagreement between experimental data and fit at lower wavelengths in **Figure 5**.

Figure 7 shows the results obtained using only one of the methods (AFM, scatterometry and Mueller ellipsometry) and the results obtained by combining more than one method. We observe that all individual methods give a fair estimate of the measurand(s), with Mueller ellipsometry having the lowest uncertainties. The combination of the three technologies is expected to improve the results obtained from **Eqs 13–15** since the three technologies measure the dimensions by probing different physical measurands. AFM measures the physical height directly through contact forces between tip and sample, scatterometry optically assesses part of the Mueller matrix element m_{11}, and normalized Mueller ellipsometry measures the rest of the Mueller matrix elements, divided by m_{11}. The direct AFM height measurement constrains the height search to a more narrow region set by the Tikhonov penalty term

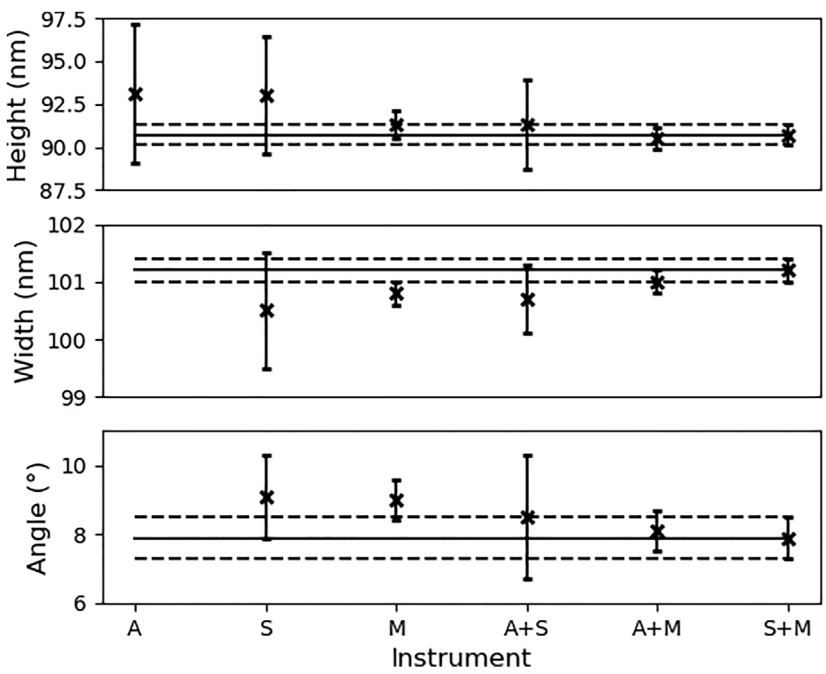

FIGURE 7 | Measurement results for the patterned silicon structure, $\Gamma_x = \Gamma_y = 200$ nm, with uncertainties. The fully drawn line corresponds to the result found by combining all instruments, and the dashed lines denote the upper and lower boundary defined by the uncertainties. The uncertainties shown are the 2σ taken at 95% confidence level. We use the abbreviations A for AFM, S for scatterometry, and M for Mueller ellipsometry in the figure. The corner roundings and the oxide layer has been locked to $R_{top} = R_{bot} = 5$ nm and $d = 2$ nm. AFM was only used for height measurement of the structures. The shown values are tabulated in **Supplementary Table S1**.

and is thus expected to influence the results if a strong correlation between grating parameters p exist in the optical measurements. We furthermore observe that the results obtained by the combination of data from more than one method show a reduced sidewall angle, whereas smaller relative variations are observed in height and width. The results obtained from combining all methods are assumed to give the most robust results, and is therefore considered to be the best estimate of the correct results. **Figure 7** shows that the combination of AFM measurement with one of the optical methods moves the sidewall angle towards the best estimate, and that the combination of AFM and Mueller ellipsometry nearly gives the best estimate. It is also evident from the figure that the combination of the two optical methods reproduces the results obtained by combining all the methods. This shows that AFM measurement with the given uncertainty does not improve the result of combined Mueller ellipsometry and scatterometry, demonstrating that the combination of the two technologies reduces the correlation between the grating parameters p.

Precise measurement of sidewall angle has become increasingly important in the semiconductor industry for high precision measurement of the full width half maximum gate linewidth [5]; with decreasing gate line-width dimension. The most common source of sidewall angle variation is photoresist exposure due to focus variation. The sidewall angle is not well monitored by top-down CD-SEMs, which is typically employed to measure the top gate line-width [6]. Inverse modeling techniques like Mueller ellipsometry and scatterometry has an advantage by enabling complete sample profile control that allows simultaneous monitoring of height, width and sidewall angle. This work suggests that non-normalized Mueller ellipsometry in the form of combined Mueller ellipsometry and scatterometry is the optimal solution since it gives the same results as data fusion between AFM, Mueller ellipsometry and scatterometry. In our case, this is fortunate since scatterometry can be performed in the Mueller ellipsometry setup without moving the sample and at nearly no additional time cost. This work furthermore emphasizes the need for the development and calibration of an automated non-normalized Mueller ellipsometer for precision metrology inspection of nanostructures.

4 CONCLUSION

In the current work, the importance of hybrid metrology was discussed as a method for precision measurements of two dimensional periodic structures. We have presented and demonstrated the use of new and improved formulas for high precision Mueller ellipsometry. The analysis was carried out by setting up a regression problem that minimizes a χ^2 loss function. The input to the loss function could be data from a single instrument or data from multiple instruments. The analysis demonstrates that data fusion from multiple instruments can be used to reduce the correlation between the dimensional parameters measured by the optical methods. The results for non-normalized Mueller ellipsometry, combination of scatterometry and normalized Mueller ellipsometry, is particularly interesting since it gives more accurate results than the other methods and the same accuracy as applying all hybrid methods. This demonstrates that non-normalized Mueller ellipsometry is a versatile method for periodic nanostructure reconstruction. The results also demonstrated that parameters such as sidewall angle, that were highly correlated for only one instrument, became less correlated if data for more instruments were analyzed together, making it possible to determine these parameters with higher accuracy. This study also suggests that at a certain point you do not get any improvement by adding input from more instruments if you already have found the best possible parameter set. The results of this work demonstrate that the developed method is capable of meeting the demands of height and width uncertainties less than 1 nm. This paper has also put great emphasis on instrument calibration, since it is very important for precision measurements. Finally, it has been demonstrated that the polarization ellipsoid obtained from Mueller ellipsometry can be used to determine the anisotropic shape of the geometrical structure, giving a better understanding of the data than if only scatterometry data is available.

DATA AVAILABILITY STATEMENT

The raw data supporting the conclusions of this article will be made available by the authors, without undue reservation.

AUTHOR CONTRIBUTIONS

PEH: RCWA theory and code writing. Calibration theory and code writing, inverse modelling theory, Mueller ellipsometer measurements, writing the paper. SRJ Discussing results and performing AFM measurements. SAJ Discussing results and writing the paper. JSMM: Mueller ellipsometer measurements, scatterometry measurements, inverse modelling coding and optimization, writing the paper.

FUNDING

This project has received funding from the Danish Agency for Institutions and Educational Grants and the EMPIR project 15SIB09 3DNano. The EMPIR program is co-financed by the Participating States and from the European Union's Horizon 2020 research and innovation program. PEH and SAJ were supported by the Danish Agency for Institutions and the EMPIR projects 17FUN01 BeCOMe and 20FUN02 POLight, both cofinanced by the Participating States and from the European Union's Horizon 2020 research and innovation programme.

SUPPLEMENTARY MATERIAL

The Supplementary Material for this article can be found online at: https://www.frontiersin.org/articles/10.3389/fphy.2021.791459/full#supplementary-material

REFERENCES

1. Pan C, Liu Z, Pang Y, Zheng X, Cai H, Zhang Y, et al. (2018). Design of a High-Performance In-Coupling Grating Using Differential Evolution Algorithm for Waveguide Display. *Opt Express* 26, 26646–62. doi:10.1364/OE.26.026646
2. Lee W, Park S-J (2014). Porous Anodic Aluminum Oxide: Anodization and Templated Synthesis of Functional Nanostructures. *Chem Rev* 114, 7487–556. doi:10.1021/cr500002z
3. Bernd MGS, Bragança SR, Heck N, Filho LCd. S. Synthesis of Carbon Nanostructures by the Pyrolysis of wood Sawdust in a Tubular Reactor. *J Mater Res Technol* (2017) 6:171–7. doi:10.1016/j.jmrt.2016.11.003
4. VK Tewary, editor. *Modeling, Characterization, and Production of Nanomaterials*. Amsterdam: No. Number 73 in Woohead Publishing series in electronic and optical materialsElsevier (2015).
5. Bingham PR, Price JR, Tobin KW, Karnowski TP, Bennett MH, Bogardus EH, et al. Sidewall Structure Estimation from CD-SEM for Lithographic Process Control. In: KWT Jr. I Emami, editors. *Process and Materials Characterization and Diagnostics in IC Manufacturing*, 5041. Santa Clara, CA: International Society for Optics and Photonics (SPIE Event: Advanced Microelectronic Manufacturing) (2003). p. 115–26. doi:10.1117/12.485229
6. Lee H, Ranjan A, Prager D, Bandy KA, Meyette E, Sundararajan R, et al. *Advanced Profile Control and the Impact of Sidewall Angle at Gate Etch for Critical Nodes*. California, USA): San Jose (2008). p. 69220T. doi:10.1117/12.774962
7. Wurm M, Endres J, Probst J, Schoengen M, Diener A, Bodermann B. Metrology of Nanoscale Grating Structures by UV Scatterometry. *Opt Express* (2017) 25:2460. doi:10.1364/OE.25.002460
8. Chen X, Liu S, Zhang C, Jiang H, Ma Z, Sun T, et al. Accurate Characterization of Nanoimprinted Resist Patterns Using Mueller Matrix Ellipsometry. *Opt Express* (2014) 22:15165. doi:10.1364/OE.22.015165
9. Raymond C. Overview of Scatterometry Applications in High Volume Silicon Manufacturing. In: AIP Conference Proceedings, 788 (2005). p. 394–402. doi:10.1063/1.2062993
10. Moharam MG, Gaylord TK. Rigorous Coupled-Wave Analysis of Planar-Grating Diffraction. *J Opt Soc America* (1981) 71:811–8. doi:10.1364/JOSA.71.000811
11. Madsen MH, Hansen P-E. Scatterometry—fast and Robust Measurements of Nano-Textured Surfaces. *Surf Topography: Metrology Properties* (2016) 4: 023003–28. doi:10.1088/2051-672X/4/2/023003
12. Garcia-Caurel E, De Martino A, Gaston J-P, Yan L. Application of Spectroscopic Ellipsometry and Mueller Ellipsometry to Optical Characterization. *Appl Spectrosc* (2013) 67:1–21. doi:10.1366/12-06883
13. Compain E, Poirier S, Drevillon B. General and Self-Consistent Method for the Calibration of Polarization Modulators, Polarimeters, and Mueller-Matrix Ellipsometers. *Appl Opt* (1999) 38:3490. doi:10.1364/AO.38.003490
14. Jellison GE, Modine FA. Two-modulator Generalized Ellipsometry: experiment and Calibration. *Appl Opt* (1997) 36:8184. doi:10.1364/AO.36.008184
15. Tompkins HG, Irene EA. *Handbook of Ellipsometry*. Norwich: William Andrew Publishing (2005).
16. Arteaga O, Freudenthal J, Wang B, Kahr B. Mueller Matrix Polarimetry with Four Photoelastic Modulators: Theory and Calibration. *Appl Opt* (2012) 51: 6805–17. doi:10.1364/AO.51.006805
17. Hansen P-E, Madsen MH, Lehtolahti J, Nielsen L. Traceable Mueller Polarimetry and Scatterometry for Shape Reconstruction of Grating Structures. *Appl Surf Sci* (2017) 421:471–9. doi:10.1016/j.apsusc.2017.02.091
18. Fry ES, Kattawar GW. Relationships between Elements of the Stokes Matrix. *Appl Opt* (1981) 20:2811. doi:10.1364/AO.20.002811
19. Gil JJ, Bernabeu E. A Depolarization Criterion in Mueller Matrices. *Optica Acta Int J Opt* (1985) 32:259–61. doi:10.1080/713821732
20. Goldstein DH. *Polarized Light*. 3rd edn. Boca Raton: CRC Press (2011). p. 3.
21. Garnaes J, Kofod N, Kühle A, Nielsen C, Dirscherl K, Blunt L. Calibration of Step Heights and Roughness Measurements with Atomic Force Microscopes. *Precision Eng* (2003) 27:91–8. doi:10.1016/S0141-6359(02)00184-8
22. Hansen P-E, Nielsen L. Combined Optimization and Hybrid Scalar–Vector Diffraction Method for Grating Topography Parameters Determination. *Mater Sci Eng B* (2009) 165:165–8. doi:10.1016/j.mseb.2009.09.006
23. Richter I, Sun P-C, Xu F, Fainman Y. Design Considerations of Form Birefringent Microstructures. *Appl Opt* (1995) 34:2421. doi:10.1364/AO.34.002421
24. Arwin H, Magnusson R, Landin J, Järrendahl K. Chirality-induced Polarization Effects in the Cuticle of Scarab Beetles: 100 Years after Michelson. *Philos Mag* (2012) 92:1583–99. doi:10.1080/14786435.2011.648228
25. Hansen P-E, Madsen JS. Thickness and Refractive index Analysis of Ellipsometry Data of Ultra-thin Semi-transparent Films. In: *Imaging and Applied Optics 2018*, 24. JM4A: Optical Society of America (2018).

Conflict of Interest: The authors declare that the research was conducted in the absence of any commercial or financial relationships that could be construed as a potential conflict of interest.

Publisher's Note: All claims expressed in this article are solely those of the authors and do not necessarily represent those of their affiliated organizations, or those of the publisher, the editors and the reviewers. Any product that may be evaluated in this article, or claim that may be made by its manufacturer, is not guaranteed or endorsed by the publisher.

Copyright © 2022 Hansen, Johannsen, Jensen and Madsen. This is an open-access article distributed under the terms of the Creative Commons Attribution License (CC BY). The use, distribution or reproduction in other forums is permitted, provided the original author(s) and the copyright owner(s) are credited and that the original publication in this journal is cited, in accordance with accepted academic practice. No use, distribution or reproduction is permitted which does not comply with these terms.